


Research Paper

Novel Cs-Based Upconversion Nanoparticles as Dual-Modal CT and UCL Imaging Agents for Chemo-Photothermal Synergistic Therapy

Yuxin Liu[†], Luoyuan Li[†], Quanwei Guo, Lu Wang, Dongdong Liu, Ziwei Wei, Jing Zhou 

Department of Chemistry, Capital Normal University, No.105 Xi San Huan Road, Beijing 100048, P. R. China.

[†] These authors contribute equally in this work. Corresponding author: jingzhou@cnu.edu.cn (J. Zhou)© Ivyspring International Publisher. Reproduction is permitted for personal, noncommercial use, provided that the article is in whole, unmodified, and properly cited. See <http://ivyspring.com/terms> for terms and conditions.

Received: 2016.01.28; Accepted: 2016.05.06; Published: 2016.06.17

Abstract

Lanthanide-based contrast agents have attracted increasing attention for their unique properties and potential applications in cancer theranostics. To date, many of these agents have been studied extensively in cells and small animal models. However, performance of these theranostic nanoparticles requires further improvement. In this study, a novel CsLu₂F₇:Yb,Er,Tm-based visual therapeutic platform was developed for imaging-guided synergistic cancer therapy. Due to the presence of the heavy alkali metal Cesium (Cs) in host lattice, the nanoplatform can provide a higher resolution X-ray CT imaging than many other reported lanthanide-based CT contrast agents. Furthermore, by using the targeted RGD motif, chemotherapy drug alpha-tocopheryl succinate (α -TOS), and photothermal coupling agent ICG, this nanoplatform simultaneously provides multifunctional imaging and targeted synergistic therapy. To demonstrate the theranostic performance of this novel nanoplatform *in vivo*, visual diagnosis in the small animal model was realized by UCL/CT imaging which was further integrated with targeted chemo-photothermal synergistic therapy. These results provided evidence for the successful construction of a novel lanthanide-based nanoplatform coupled with multimodal imaging diagnosis and potential application in synergistic cancer theranostics.

Key words: CsLu₂F₇, UCL, CT, chemotherapy, photothermal therapy, synergistic therapy

Introduction

Cancer is a serious health problem and a major medical challenge worldwide. The integration of cancer diagnosis and treatment is important for dealing with this increasingly serious problem. Many nanoplatforms for simultaneous diagnosis and treatment of cancer have been reported. However, the contrast ratio of diagnosis and treatment effect remains to be improved.

Among available diagnosis modalities, computed tomography (CT) shows the best spatial and density resolutions (>50 μ m) with three-dimensional (3D) tomography of the anatomic details with high tissue penetration [1]. Nevertheless,

compared to optical imaging, CT imaging is limited in providing real-time dynamic imaging information. For further more accurate diagnosis, a combination of CT and optical imaging modalities as well as the development of multifunctional imaging agents are required. Rare-earth nanoparticles (UCNP) with a unique upconversion luminescence (UCL) mechanism can meet these demands because of their specific advantages, such as no photobleaching, absence of autofluorescence from the biosome, and outstanding light penetration depth into soft tissues [2-8]. Also, rare earth-based UCNPs with a high X-ray mass attenuation coefficient (2.32 - 4.01 cm² g⁻¹) can be

applied as a CT contrast agent. Among alkali metal sources, cesium (Cs) theoretically has a higher X-ray absorption coefficient than that of other common alkali metals, because X-ray attenuation properties are positively related to molecular weight. Therefore, a Cs-based UCNP may be an effective CT/UCL dual model agent for cancer diagnosis and localization.

The treatment effect should also be improved and optimized after diagnosis. Photothermal therapy (PTT) is a novel emerging cancer treatment that can inhibit the growth of cancer cells and ablate tumors using therapeutic photothermal agents exposed to a near-infrared laser (NIR), which results in higher temperatures surrounding the tumor. Currently, the available PTT coupling agents mainly include metal nanoparticles [9-10], semiconductor nanoparticles [11-14], carbon-based nanomaterials [15-16], polymeric nanoparticles [17-22], and a small-molecule dye indocyanine green (ICG) [23-26], which is a hydrophilic photothermal agent approved by the U.S. Food and Drug Administration. However, PTT alone fails inevitably resulting in tumor recurrence and metastasis because of the nonhomogeneous heat distribution within the tumor tissue [27]. Conventional chemotherapy plays a crucial role, as it is more acceptable to patients and inhibits metastatic spread in the body. Therefore, a combination of PTT and chemotherapy, known as photothermal-chemo synergistic therapy, shows a better therapeutic effect than each treatment alone [28-29]. Previous studies of the biological antitumor activity of non-common chemotherapeutic drugs showed that alpha-tocopheryl succinate (*α*-TOS), a vitamin E derivative, selectively inhibits cell proliferation and induces apoptosis of many different types of cancer cells, but not normal cells [30]. These effects are based on the action of complex extracellular and intracellular signal transduction pathways that trigger tumor cell apoptosis, inhibition of DNA synthesis, and tumor cell differentiation.

In this study, we designed a multifunctional UCNP, a nanoplatfrom that integrates cancer diagnosis and chemo-photothermal therapy. This is accomplished by using CsLu₂F₇:Yb,Er,Tm as a CT/UCL contrast agent, RGD peptide as an active targeting molecule, *α*-TOS as a chemotherapy drug, and ICG as a PTT agent. Following intravenous injection of the UCNPs in tumor-bearing mouse models, CT/UCL imaging was used to visualize the location of the tumor in the body. The synergistic therapeutic effect in cultured cells and small-animal models was also investigated. In addition, the biocompatibility of the multifunctional nanoplatfrom was evaluated.

Experimental Section

Materials

All the starting materials were obtained from commercial supplies and used as received. Rare-earth oxides Lu₂O₃ (99.999%), Yb₂O₃ (99.999%), Er₂O₃ (99.999%), and Tm₂O₃ (99.99%) were purchased from Beijing Lansu Co. Ltd. RECl₃ (RE³⁺ = Lu³⁺, Yb³⁺, Er³⁺, Tm³⁺) was prepared by dissolving the corresponding metal oxide in hydrochloric acid at elevated temperature then removed the solvent. Ethanol, cyclohexane, toluene, and hydrochloric solution were purchased from Sinopharm Chemical Reagent Co. China. Oleic acid (OA) (>90%) and 1-octadecene (ODE) were purchased from Aldrich. CsOH·H₂O was purchased from Alfa Aesar Ltd. Indocyanine green (ICG) were purchased from TCI Chemical Reagent Shanghai Co. Ltd. Alpha-tocopheryl succinate (*α*-TOS) and N-hydroxysuccinimide sodium salt (sulfo-NHS) were purchased from Sigma (St. Louis, MO). DSPE-PEG (2000) maleimide and DSPE-PEG (2000) amino were purchased from Avanti. 1-ethyl-3-(3-dimethylaminopropyl) carbodiimide hydrochloride (EDC) was purchased from Aladdin Reagent Co. Ltd. All the other chemical reagents were of analytical grade and were used directly without further purification. Deionized water was used throughout.

Synthesis of UCNP-ICG-TOS-RGD

Synthesis of oleic acid (OA)-coated upconversion nanoparticles (UCNP-OA)

UCNP-OA was synthesized according to the reference with some modification.[31] A typical procedure is as follow: given amounts of LuCl₃ (0.78 mmol), YbCl₃ (0.20 mmol), ErCl₃ (0.016 mmol), and TmCl₃ (0.004 mmol) were added to a 100 mL three-necked flask containing OA (6 mL) and ODE (15 mL). The mixture was heated to 160°C to form a pellucid solution, and then cooled down to room temperature. 10 mL of methanol solution containing CsOH·H₂O (2.5 mmol) and NH₄F (4 mmol) was slowly dropped into the flask and stirred for 30 min. Subsequently, the solution was heated to 295°C and maintained for 1 h at argon atmosphere. After the solution was cooled naturally, an excessive amount of ethanol was poured into the resultant mixture was centrifugally separated, and the products were collected and washed with cyclohexane and ethanol three times.

Synthesis of DSPE-PEG (2000) maleimide/amino-functionalized upconversion nanoparticles (UCNP-PEG)

DSPE-PEG (2000) maleimide, DSPE-PEG (2000)

amino, and UCNP-OA according to the mass ratio 1:1:2 were dispersed separately in chloroform and then mixed together. After stirred for 2 h, the chloroform was evaporated. The product was collected *via* 10000 rpm centrifugation for 5 min and washed with deionized water for three times. The product, named UCNP-PEG, was dispersed easily in deionized water.

Synthesis of indocyanine green (ICG)-functionalized upconversion nanoparticles with targeting molecules (UCNP-ICG-RGD)

The UCNP-ICG with adding targeting molecules was prepared using aqueous-based preparation method.[32-33] ICG (1 mmol) was added to HEPES (4-(2-hydroxyethyl)-1-piperazineethanesulfonic acid) buffer (0.1 M, 5 mL, pH = 8.0) containing the UCNP-PEG (1 mmol) and stirred for 8 h at room temperature. The precipitate (UCNP-ICG) was obtained after 5 min 10000 rpm centrifugation and washing with deionized water to remove excess nonbinding ICG. Then, the 6-maleimidohexanoic acid NHS (30 mg, 0.97 mmol) was added to HEPES buffer of c(RGDFK) (69 mg, 1 mmol). The reaction was allowed to stir gently overnight at room temperature. After washing and centrifugation, UCNP-ICG-RGD were obtained and suspended in HEPES buffer (0.1 M, 5 mL, pH = 7.3) and stored at 4°C.

Synthesis of RGD/TOS-functionalized upconversion nanoparticles (UCNP-TOS-RGD)

α -TOS (1 mmol) was mixed with a dimethylsulfoxide (DMSO) solution (2 mL) containing EDC (0.01 mmol), sulfo-NHS (0.092 mmol), and the mixture was stirred for 3 h. Similar to the previous method [9], the precipitate and DMSO solution of α -TOS were added to HEPES buffer (0.1 M, 5 mL, pH = 7.3) of c(RGDFK) (1 mmol). The mixed solutions were stirred gently overnight at room temperature. After centrifugation and washing three times with deionized water, UCNP-TOS-RGD were obtained and suspended in HEPES buffer (0.1 M, 5 mL, pH = 7.3) and stored at 4°C.

Synthesis of UCNP-ICG-TOS-RGD

Similar to the above method, the HEPES buffer of UCNP-ICG-RGD was added to a DMSO solution of α -TOS (1 mmol), and the mixture was stirred 8 h at room temperature. The UCNP-ICG-TOS-RGD were obtained by washing three times with deionized water and stored in HEPES buffer (0.1 M, 5 mL, pH = 7.3) at 4°C.

Characterization

Sizes and morphologies were determined at 200 kV using a JEOL JEM-2010F high-resolution

transmission electron microscope (HR-TEM). Energy-dispersive X-ray analysis (EDXA) was also performed during HR-TEM measurements. Dynamic light scattering experiments were carried out on a Zetasizer nano 90. Powder X-ray diffraction (XRD) measurement was measured with a Bruker D4 X-ray diffractometer (Cu K α radiation, 0.15406 nm). Upconversion luminescence (UCL) spectra were measured with a Maya LIFS-980 fluorescence spectrometer by using an external 0-5 W 980 nm adjustable laser as the excitation source. Ultraviolet-visible-near infrared (UV-vis-NIR) absorption spectra were obtained using a UV-2550 spectrophotometer (S-1700, Shimadzu, Japan). Fourier transform infrared (FTIR) spectra were performed on Fourier Transform Infrared Spectrophotometer IRPRESTIGE-21 (Shimadzu).

Cell culture

HeLa (human cervical carcinoma), U87MG (human glioblastoma), and HEK 293T (human embryonic kidney epithelial cell line) cell lines were provided by the Institute of Basic Medical Sciences Chinese Academy of Medical Sciences. Cells were grown in DMEM (Dulbecco's modified Eagle's medium) supplemented with 10% FBS (fetal bovine serum) and 1% penicillin-streptomycin at 37°C with 5% CO₂. Cultures were maintained at 37°C under a humidified atmosphere containing 5% CO₂. For use in the experiments, 1×10^5 cells well⁻¹ were seeded in 10 mm glass coverslips and allowed to attach for 24 h prior to the assay. To generate HeLa cells with low $\alpha_v\beta_3$ -integrin density, HeLa cells were passaged using trypsin but not scarping.

Toxicology studies

MTT assays

U87MG cells were seeded into a 96-well cell culture plate at 5×10^5 well⁻¹, under 100% humidity, and were cultured at 37°C and 5% CO₂ for 24 h; the different concentrations of UCNP-ICG-RGD (0, 400, 600, 800, 1000, and 1200 $\mu\text{g mL}^{-1}$ diluted in RPMI 1640) were then added to the wells. The cells were subsequently incubated for 4 h or 24 h at 37°C under 5% CO₂. Thereafter, 3-(4,5-Dimethylthiazol-2-yl)-2,5-diphenyltetrazolium bromide (MTT, 10 μL ; 5 mg mL⁻¹) was added to each well and the plate was incubated for an additional 4 h at 37°C under 5% CO₂. After the addition of DMSO (100 μL well⁻¹), the assay plate was allowed to stand at room temperature for 12 h. The optical density OD570 value (*Abs.*) of each well, with background subtraction at 690 nm, was measured by means of a Tecan Infinite M200 monochromator-based multifunction microplate reader. The following formula was used to calculate

the inhibition of cell growth:

$$\text{Cell viability (\%)} = (\text{mean of Abs. value of treatment group} / \text{mean Abs. value of control}) \times 100\%.$$

Histology and hematology studies

This work with animals was in accordance with the protocol as approved by IACUC (Institutional Animal Care and Use Committee). Blood samples and tissues were harvested from test (intravenous injection of the UCNP-ICG-RGD) and control (no injection of the UCNP-ICG-RGD) group of nude mice ($n = 5$) after 30 min, 24 h, 7 d, and 30 d. Blood was collected from the orbital sinus by quickly removing the eyeball from the socket with a pair of tissue forceps. Five important hepatic indicators (alanine aminotransferase: ALT, aspartate aminotransferase: AST, total bilirubin: TBIL, total protein: TP, albumin: ALB), and two indicators for kidney functions (creatinine: CREA and urea: UA) were measured. The serum chemistry data were measured in Nanjing Biomedical Research Institute of Nanjing University. Upon completion of the blood collection, mice were sacrificed. Heart, liver, spleen, lung, kidney, intestine, and stomach were removed, and fixed in paraformaldehyde, embedded in paraffin, sectioned, and stained with hematoxylin and eosin (H&E). Long-term toxicity of the UCNP-ICG-RGD was further investigated over 30 days by histology studies.

Tumor xenografts

This work with animals was in accordance with the protocol approved by IACUC (Institutional Animal Care and Use Committee). Tumor cells were harvested when they reached near confluence by incubating with 0.05% trypsin-EDTA. U87MG cells were pelleted by centrifugation and resuspended in sterile phosphate-buffered saline (PBS). Cells (5×10^6 cells site⁻¹) were implanted subcutaneously into the right hind leg of four-week-old female athymic NU/NU nude mice. Biodistribution and imaging studies were performed when tumors reached 4-6 mm in average diameter (3 weeks after implant).

Targeted efficiency

Flow cytometric analysis: U87MG and HeLa cells (1×10^6 cells) were washed with ice-cold PBS, and then resuspended in $\alpha_v\beta_3$ PBS solution (1%) and cultured in an ice-cold environment for another 30 min. The cells were analyzed in a flow cytometer. A minimum of 10000 events were examined for each sample.

Biodistribution: All the animal procedures were in agreement with IACUC and carried out ethically and humanely. 12 tumor-bearing nude mice were used to study the biodistribution of UCNP,

UCNP-ICG, UCNP-ICG-RGD; 3 mice each were in test groups 1 and 2 injected with UCNP (200 μL , 1 mg mL⁻¹) and UCNP-ICG (200 μL , 1 mg mL⁻¹), respectively and 6 mice in test group 3 and 4 were injected with UCNP-ICG-RGD (200 μL , 1 mg mL⁻¹). The 3 mice in test group 1, 2, and 3 were sacrificed 24 hours post-injection while the 3 mice in test group 4 were sacrificed 48 hours post-injection. The heart, liver, spleen, lung, and kidneys were harvested, taken up in DI water (1 mL), centrifuged, and the supernatant diluted with DI water to 1:10 v/v. Determination of Lu uptake content in tissues and excrements were performed by inductively coupled mass spectroscopy (ICP-MS) analysis (Agilent 7500ce ICP-MS).

Targeted computed tomography (CT)

In vitro: Various mass concentrations of NaLuF₄- and CsLu₂F₇-based nanoparticles (0.75, 1.5, 3, 6 and 12 mg mL⁻¹) dispersed in deionized water were prepared in a series of 1.5 mL tubes for phantom test. CT images were acquired using a dual-source CT system (SIEMENS Inveon MMCT micro CT instrument). Imaging parameters were as follows: effective pixel size, 53.01 μm ; 70 KVp, 500 μA ; field of view, 54.28 mm \times 81.42 mm; rotation steps, 180; binning, 2; exposure time, 200 ms rotation⁻¹. Images of phantom CT images were analyzed with Kodak Molecular Imaging Software. Hounsfield unit (HU) values were measured by the SIEMENS Inveon MMCT micro CT software.

In vivo: NU/NU mice were anesthetized (with 10% chloral hydrate, 100 μL) and were injected intravenously with the UCNP-ICG-RGD solution (200 μL , 1 mg mL⁻¹). 30 min post-injection, whole-body imaging was performed. Effective pixel size, 52.81 μm ; 80 KVp, 500 μA ; field of view, 54.07 mm \times 81.11 mm; rotation steps, 180; binning, 2; exposure time, 600 ms rotation⁻¹.

Targeted upconversion luminescence (UCL) imaging

In vitro: For cell staining assays, U87MG and HeLa cells were incubated with the UCNP-ICG-RGD (300 $\mu\text{g mL}^{-1}$) for 1 h at 37°C in a serum-free medium. U87MG cells were employed for targeted UCL imaging, whereas the HeLa cells were used in the control experiments. For comparison, U87MG cells were also incubated with non-RGD conjugated UCNP-ICG (300 $\mu\text{g mL}^{-1}$); U87MG cells were incubated with excess free RGD (50 μL ; 1 mM) and then incubated with UCNP-ICG (300 $\mu\text{g mL}^{-1}$) under otherwise identical conditions. Excitation of the cells was provided by the continuous wave (CW) laser at 980 nm; the green and red UCL emission of

UCNP-RGD was collected at 530 ± 30 nm and 650 ± 50 nm, respectively.

In vivo: The same mice used in CT imaging were then transferred to a UCL system for UCL imaging. And then tissues (heart, lung, tumor, liver, spleen, and kidney) dissected from these mice were used for targeted UCL imaging. The UCL imaging was performed with a modified upconversion luminescence *in vivo* imaging system designed as described in literature [43]. *In vivo* UCL signals were collected at 800 ± 12 nm.

Targeted photothermal imaging

In vitro: Photothermal imaging was performed with FLIR E40 equipment, in conjunction with an 808 nm laser illuminator, which was set up by our group [20]. Dilutions of UCNP-ICG-RGD in deionized water (100 - 1000 $\mu\text{g mL}^{-1}$) were placed in specimen bottles irradiated by an 808 nm laser (0.5 W cm^{-2}). The temperature signals recorded at different time intervals (0 - 300 s) were analyzed with FLIR tools systems.

In vivo: NU/NU nude mice bearing tumor were anesthetized (with 10% chloral hydrate, 100 μL) and PBS solution of UCNP-ICG-RGD (200 μL , 1 mg mL^{-1}) was intravenously injected ($n = 5$). After irradiation by the laser of 808 nm (0.5 W cm^{-2}), temperature signals were recorded at different time points (0 - 300 s). The PBS solution of UCNP-ICG-RGD (200 μL , 1 mg mL^{-1}) was intravenously injected into the mice which were exposed to 808 nm laser (0.5 W cm^{-2}) for 10 min every other day.

Therapeutic techniques *in vitro*

To evaluate the targeted cancer cell inhibition efficiency, an MTT assay was performed following chemotherapy with UCNP-TOS-RGD, photothermal therapy with UCNP-ICG-RGD, and synergistic therapy with UCNP-ICG-TOS-RGD. Briefly, 1×10^5 U87MG (cancer cells) and 293T cells (normal cells) per well were seeded into 96-well plates overnight at 37°C and 5% CO_2 for therapeutic effect assay. For each nanomaterial, the mean and standard deviation from triplicate 96-well plates were analyzed and reported.

Chemotherapy *in vitro*: Cells were seeded into a 96-well cell culture plate at 5×10^5 well $^{-1}$, under 100% humidity, and were cultured at 37°C and 5% CO_2 for 24 h. Then, the medium of U87MG cells was replaced with fresh medium containing UCNP-TOS-RGD at different *a*-TOS dose of (0, 10, 20, 30, and 40 μM), and incubated for another 24 h. The U87MG and 293T cells were treated with free *a*-TOS and UCNP-PEG as controls.

Photothermal therapy *in vitro*: The medium of U87MG cells was replaced with fresh medium

containing UCNP-ICG-RGD at different free ICG dose of (0, 5, 10, 15, and 20 μM) under an 808 nm laser, and incubated for another 24 h. The U87MG cells treated with medium containing ICG at the same concentration upon irradiation at 808 nm laser served as a control.

Synergistic therapy *in vitro*: The medium of U87MG cells was replaced with fresh medium containing UCNP-ICG-TOS-RGD (2000 $\mu\text{g mL}^{-1}$) under an 808 nm laser, and incubated for another 24 h (Synergistic group). The U87MG cells were treated with UCNP-TOS-RGD (Chemo group), and UCNP-ICG-RGD under an 808 nm laser (Photothermal group) served as controls.

Synergistic therapy *in vivo*

When the tumor size reached 4-6 mm, nude mice bearing U87MG tumors were randomly divided in three groups ($n = 5$). Synergistic group: nude mice were intravenously injected with 200 μL of UCNP-ICG-TOS-RGD (1 mg mL^{-1}) and irradiated by 808 nm laser for 5 min. Control groups were as follows: Chemo group: mice were intravenously injected with UCNP-TOS-RGD; Photothermal group: mice were intravenously injected with UCNP-ICG-RGD and exposed to the 808 nm laser. Blank group: mice were intravenously injected with 200 μL of fresh medium. The tumors were measured by a caliper every three days after photothermal treatment and the sizes were calculated according to the formulation: The tumor volume = (tumor length) \times (tumor width) $^2/2$. During the 9 days treatment progress, 6 times injection was taken on the mice in Synergistic group and two control groups. A representative mouse of each group was sacrificed and the tumor was excised and photographed at different time points.

Results and Discussion

Synthesis and characterization

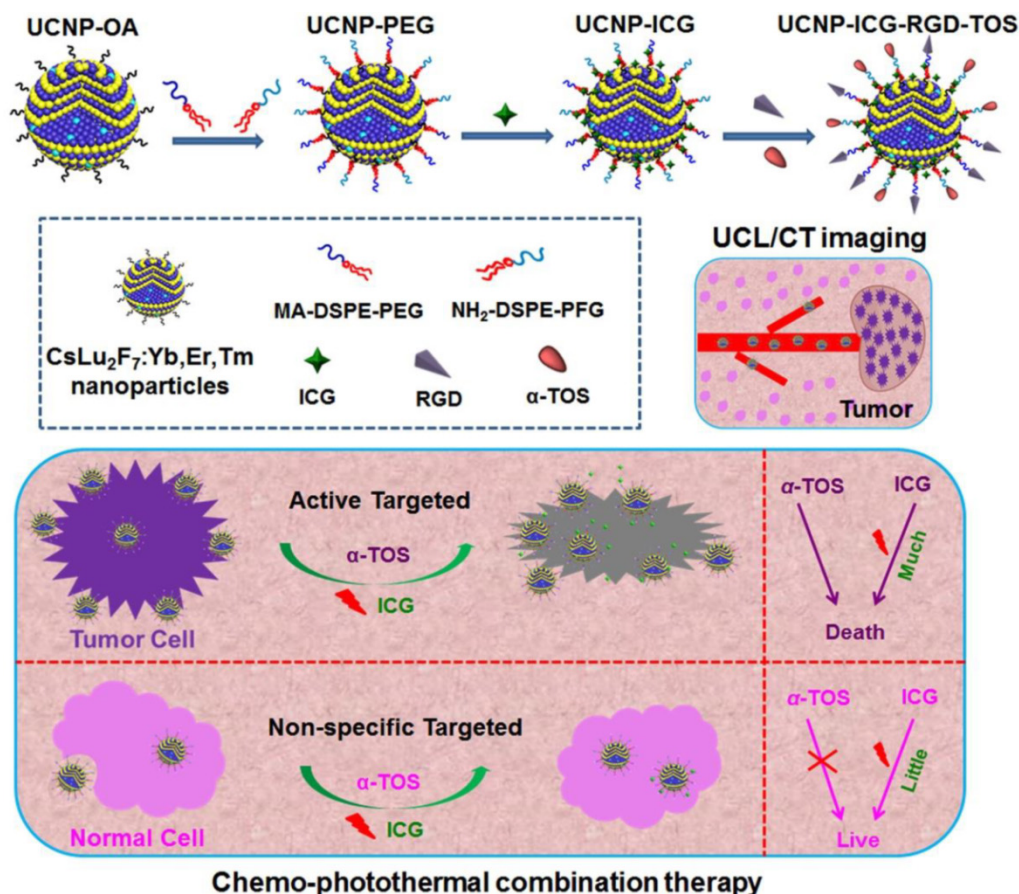
Contrary to the previous synthesis of upconversion nanoparticles, we selected Cs as the alkali metal source for UCNP. Oleic acid (OA)-capped upconversion nanoparticles (UCNP-OA) were synthesized using a modified solvothermal method (Scheme 1). The morphology and structure of the UCNP-OA were characterized by transmission electron microscopy (TEM). UCNP-OA samples were spherical in shape with a size distribution range of 10-17 nm (Figure 1A, B, & D) and did not show significant aggregation. Energy dispersive X-ray analysis (EDXA) displayed elemental peaks related to Cs, Lu, F, and Yb, confirming detectable levels of doped ions in the nanoparticle matrix (Figure S1). High-resolution TEM (HR-TEM) images of UCNP-OA

showed that the distance between lattice fringes was 0.348 nm, corresponding to the (023) planes of the hexagonal phase (Figure 1B inset). To further confirm the composition and crystallinity, the X-ray powder diffraction (XRD) pattern of the UCNP-OA was evaluated and identified in the hexagonal phase of CsLu_2F_7 (JCPDS card No. 43-0504, Figure 1C). UCNP-OA were easily dispersed in various nonpolar organic solvents (e.g. cyclohexane, toluene, and chloroform), indicating the presence of hydrophobic OA on the surface of the nanoparticles.

For the application of UCNP-OA in bioimaging-guided therapy, the surface of hydrophobic UCNP-OA was further functionalized (Scheme 1). UCNP-OAs were converted to water-soluble nanoparticles by coating with DSPE-PEG (2000) maleimide and DSPE-PEG (2000) amino to obtain PEG-coated UCNP (UCNP-PEG). Following polymer coating, there was no significant change in morphology and size based on TEM images (Figure S2). Dynamic light scattering showed that the effective hydrodynamic diameter of UCNP-PEG was approximately 30 nm (Figure S3). The increased hydrodynamic diameter may be the result of the polymer linkage and water layer coating. The

dynamic light scattering results indicated successful coating of the polymer on the nanoparticle surface.

ICG, a photothermal coupling agent, was then incorporated into the nanoparticles (UCNP-PEG) during polymer coating, as DSPE-PEG (2000) maleimide/amino is comprised of a long lipophilic alkyl tail and hydrophilic polar head group. By measuring the absorbance at 785 nm, the ICG content in the UCNP-ICG samples was determined to be $9.62 \times 10^{-6} \text{ mol g}^{-1}$ (Figure 2A & B). The stability and leakage of ICG were also considered. No obvious ICG leakage was observed, suggesting that ICG can be stably incorporated into the UCNP (Figure S4). Moreover, based on the conjugation of maleimide groups of PEG and thiolated groups of c(RGDFK), UCNP-ICGs were coupled with the targeting functional c(RGDFK) (abbreviated as UCNP-ICG-RGD) to ensure the targeting ability to cancer cells. The fourier transform infrared (FTIR) spectra supported the successful surface modification of UCNP (Figure S5). Using the ninhydrin method, the level of RGD was determined to be $\sim 10^{-7} \text{ mol g}^{-1}$ (Figure S6).



Scheme 1. Schematic illustration of the synthesis of the ICG, α-TOS, and RGD-modified $\text{CsLu}_2\text{F}_7\text{:Yb,Er,Tm}$ multifunctional nanoplatform (UCNP-ICG-RGD-TOS) and their targeted chemo-photothermal synergistic therapy of tumor cells.

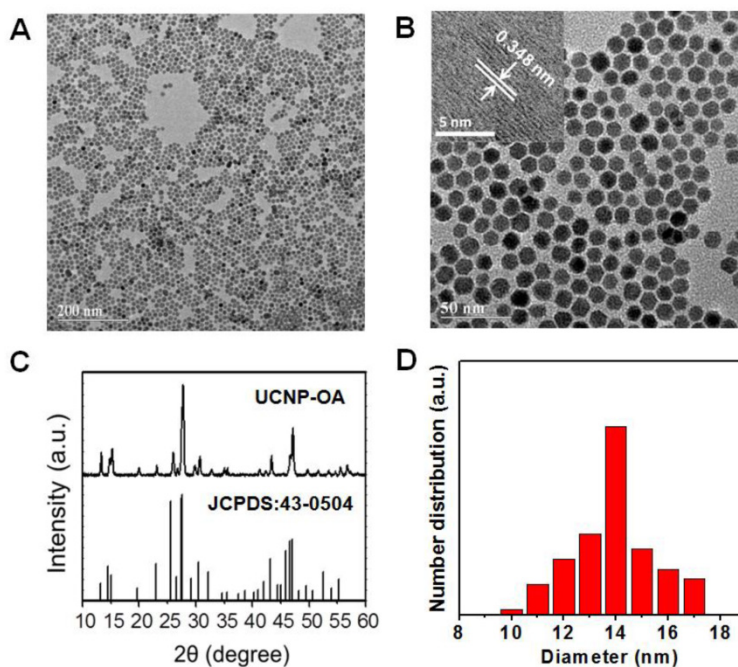


Figure 1. TEM images of the UCNPs-OA. (A) Scale bar: 200 nm. (B) Scale bar: 50 nm. Inset: the HR-TEM image of UCNPs-OA. (C) XRD pattern of UCNPs-OA and standard card of its hexagonal phase (JCPDS card No. 43-0504). (D) Size distribution of UCNPs-OA in cyclohexane.

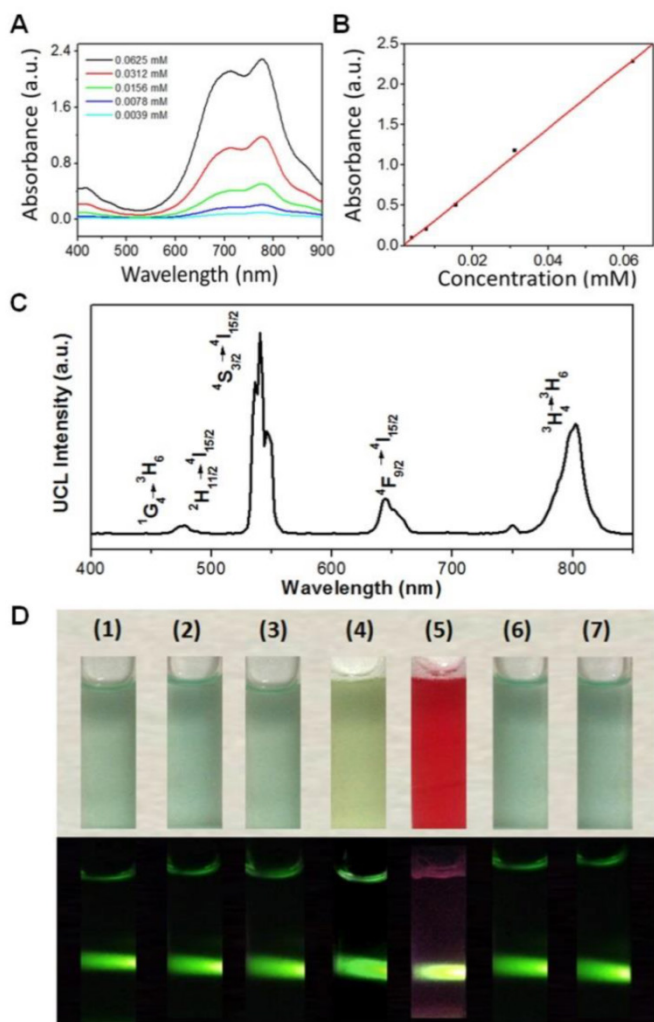


Figure 2. (A) Absorption spectra of UCNPs-ICG solution and standard solutions containing different concentrations of ICG. (B) ICG concentration vs absorption at $\lambda = 805$ nm. (C) Room temperature UCL emission spectrum of UCNPs-ICG-RGD dissolved in water (1 mg mL^{-1}) under CW excitation with a 980 nm laser (power of 800 mW). (D) Photographs (top) and UCL images (bottom) of UCNPs-ICG-RGD dissolved in various solutions: (1) water, (2) phosphate-buffered saline (PBS), (3) 5% glucose solution, (4) fetal bovine serum (FBS), (5) Dulbecco modified Eagle medium (DMEM), (6) 0.9% NaCl solution, and (7) artificial cerebrospinal fluid.

The UCL emission spectrum of the UCNPs-ICG-RGD (78%mol Lu, 20%mol Yb, 1.6%mol Er, 0.4%mol Tm) in water (1 mg mL^{-1}) at room temperature is shown in Figure 2C. Under continuous-wave (CW) excitation at 980 nm, UCNPs-ICG-RGD exhibited distinct UCL emission bands at 520, 540, and 654 nm, corresponding to the $^2\text{H}_{11/2} \rightarrow ^4\text{I}_{15/2}$, $^4\text{S}_{3/2} \rightarrow ^4\text{I}_{15/2}$, and $^4\text{F}_{9/2} \rightarrow ^4\text{I}_{15/2}$ transitions of Er^{3+} , respectively; UCL emission bands at 490, 695, and 800 nm originated from the $^1\text{G}_4 \rightarrow ^3\text{H}_6$, $^3\text{F}_3 \rightarrow ^3\text{F}_4$, and $^3\text{H}_4 \rightarrow ^3\text{H}_6$ transitions of Tm^{3+} , respectively. The UCL emissions showed no obvious change before and after PEG surface modification. After ICG loading, the strong absorption of ICG at 785 nm slightly blocked the 800 nm emission of UCNPs, which would not influence the application of UCNPs for optical imaging (Figure S7). We further measured the solubility of UCNPs-ICG-RGDs in water and physiologically relevant solutions, including phosphate-buffered saline, 5% glucose solution, fetal bovine serum, Dulbecco modified Eagle medium, 0.9% NaCl solution, and artificial cerebrospinal fluid. Before centrifugation, no aggregates were observed in any of

the solutions and the samples exhibited UCL upon 980 nm excitation (Figure 2D). After centrifugation, the UCNP-ICG-RGDs still exhibited bright UCL upon excitation and were redispersed in the solution by ultrasonication (Figure S8). However, both water and free ICG solution showed no UCL signal under the 980 nm laser (Figure S9). These data indicate that the UCNP-ICG-RGDs had good solubility in physiologically relevant solutions and can be used as UCL imaging probes.

Toxicology studies

To evaluate the safety and possibility of using a novel material for bioapplication, toxicity should be carefully evaluated. Therefore, the *in vitro* and *in vivo* toxicities of UCNP-ICG-RGDs were examined.

In vitro: Prior to using UCNP-ICG-RGDs for *in vivo* imaging, we first tested their cytotoxicity using the methyl thiazolyltetrazolium (MTT) assay (Figure S10), which revealed no significant differences in the proliferation of U87MG cells in the absence or presence of UCNP-ICG-RGDs (0–1200 $\mu\text{g mL}^{-1}$) within 12 and 24 h. Even after 24 h incubation, cell viability was estimated to be approximately 80%. The MTT assay results demonstrated that UCNP-ICG-RGDs had low cytotoxicity to cells.

In vivo: Nanoparticles toxicity was assessed in mice. Mice intravenously injected with UCNP-ICG-RGDs (200 μL , 1 mg mL^{-1}) were sacrificed at different time intervals (30 min, 24 h, 7 d, 30 d, 45 d, and 60 d) after injection, and their organs, including the heart, liver, spleen, lung, and kidneys, were harvested for histochemical analysis. The results of histochemical studies showed no significant differences between the test and control mice at different time intervals (Figure S11). The organs showed no detectable toxicity (e.g. necrosis, hydropic degeneration, inflammatory infiltrates, pulmonary fibrosis, gastroenteritis, or infectious diarrhea), indicating the safety of UCNP-ICG-RGDs. Finally, serum biochemistry assays were performed to further evaluate toxicity in organs, particularly in the liver and kidney. Five important hepatic function indicators (alanine aminotransferase, aspartate aminotransferase, total bilirubin, total protein, and albumin) and two indicators of kidney function (creatinine and urine albumin) were analyzed (Figure S12). These indicators were in the normal range in mice injected with UCNP-ICG-RGD solution. Therefore, UCNP-ICG-RGDs had no obvious or detectable influence on the health of injected mice.

Targeted efficiency

As a targeted nanoplatform for multifunctional imaging and therapy, the target efficiency of

UCNP-ICG-RGDs was evaluated.

In vitro: Integrin $\alpha_v\beta_3$ plays a pivotal role in tumor angiogenesis and is a receptor for extracellular matrix proteins with an exposed RGD tripeptide sequence. We first systematically investigated integrin $\alpha_v\beta_3$ expression on different cells by the flow cytometric analysis using an $\alpha_v\beta_3$ -complex-specific monoclonal antibody. As shown in Figure 3A and 3B, U87MG cells showed higher levels of $\alpha_v\beta_3$ antibody staining than that in HeLa cells. These results indicate that U87MG cells expressed high levels of integrin $\alpha_v\beta_3$.

In vivo: Before application in small-animal imaging, the tissue distribution of UCNP-ICG-RGDs following intravenous injection was investigated by inductively coupled mass spectroscopy. The animals were sacrificed at 24 and 48 h post-injection. The Lu^{3+} concentration, an indicator of UCNP-ICG-RGD, in various organs was quantitatively analyzed (Figure S13). Inductively coupled mass spectroscopy analysis showed that UCNP-ICG-RGDs uptake and retention occurred primarily in the tumor, liver, and spleen, while only low levels of UCNP-ICG accumulated in the tumor. At 48 h post-injection, UCNP-ICG-RGD uptake by the tumor increased, while UCNP-PEG and UCNP-ICG uptake remained at low levels (Table S1). These data demonstrate that UCNP-ICG-RGD is a promising probe for targeting tumors in small animal models.

Targeted X-ray CT imaging

Toxicity analysis suggested that the UCNP-ICG-RGDs had no obvious toxicity in living systems and can be applied for *in vivo* application. Because X-ray CT imaging, which has been used in the clinic for many years, can provide detailed information regarding tumor location, we first tested the effect of CT imaging both *in vitro* and *in vivo*.

In vitro: Many novel CT contrast agents, such as I- [34], Au- [35], and lanthanide-[36–42] based nanoparticles, have been widely reported. Among these contrast agents, Lu-based nanoparticles show the best results, as Lu has a high X-ray absorption coefficient (4.01 $\text{cm}^2 \text{g}^{-1}$ at 100 keV) [43]. Therefore, NaLuF_4 nanoparticles as a CT contrast agent have been widely applied in CT *in vivo*. However, Cs has a higher theoretical molecular weight than that of common alkali metals (such as Li, Na, and K). Therefore, we investigated the X-ray attenuation of the obtained CsLu_2F_7 -based nanoparticles. For comparison, NaLuF_4 -based nanoparticles with the same size distribution as CsLu_2F_7 -based nanoparticles were synthesized (Figure S14 and S15). *In vitro* X-ray CT phantom images were acquired using various concentrations of NaLuF_4 - and CsLu_2F_7 -based

nanoparticles (0.75, 1.5, 3, 6, and 12 mg mL⁻¹) dispersed in deionized water. As the mass concentration of CsLu₂F₇-based nanoparticles increased, the CT enhancement signals continuously increased, which were higher than that of NaLuF₄-based nanoparticles at the same mass concentration (Figure 3C). The CT values, known as Hounsfield units (HU) value, of the CsLu₂F₇-based nanoparticles at 10 mg mL⁻¹ reached 232.2, which is higher than the value for NaLuF₄-based nanoparticles (HU = 175) and other reported CT contrast agents (HU = 138–220) [44–46] at the same mass concentration (Figure 3D and Table S2). Similar results were observed at the same molar concentration (Table S3). This can be explained by the fact that Cs has a higher X-ray absorption coefficient than that of the other common alkali metal, Na, and more Lu was located inside the matrix.

In vivo: CT imaging is a common technique for identifying tissues using CT contrast agents. By examining tissues containing elements with high atomic number, such as bone and contrast agent-containing tissues, the exact position of the tumor was confirmed by 3D CT volume-rendered images. Nude mice bearing U87MG tumors were administered UCNP-ICG-RGDs (200 μL, 1 mg mL⁻¹) *via* tail vein injection. Enhanced signals in the heart, liver, tumor, and vasculature were also observed in 3D CT volume-rendered images (Figure S16). From the images and relative CT values of mouse samples (Figure 3E and F), Cs-based UCNPs were superior to Na-based UCNPs, not only *in vitro* but also in the *in vivo* model. Therefore, because of the efficient targeting ability and excellent CT performance, UCNP-ICG-RGDs showed potential for use as a targeted CT contrast agent.

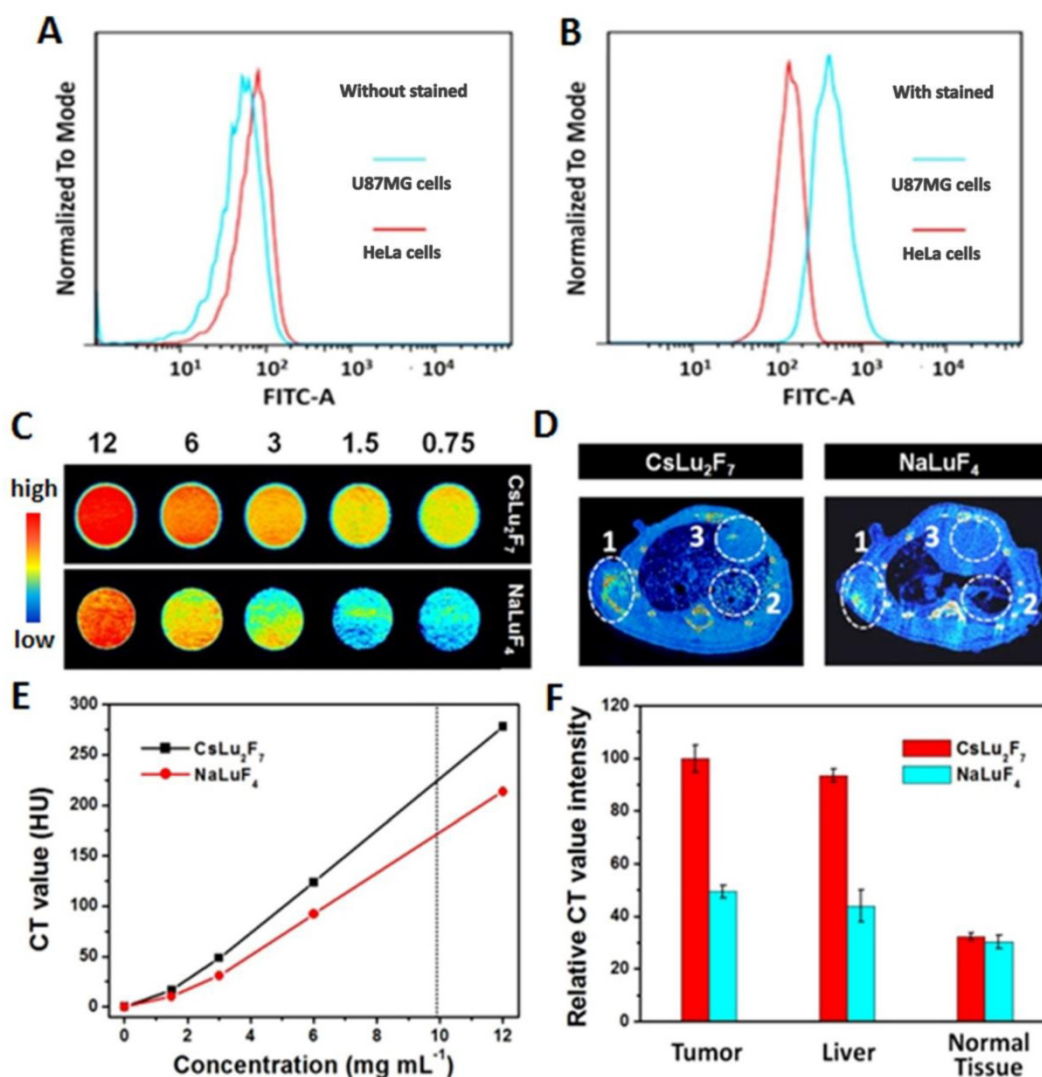


Figure 3. (A, B) Expression of integrin $\alpha_v\beta_3$ on different cells by flow cytometric analysis. (C) *In vitro* CT images Hounsfield units measurements (E) of NaLuF₄- and CsLu₂F₇-based nanoparticles with different mass concentrations of 12, 6, 3, 1.5, and 0.75 mg mL⁻¹. (D) *In vivo* maximum intensity post-injection images, and (F) relative CT value intensity of the mice were obtained 30 min post-injection of NaLuF₄- and CsLu₂F₇-based nanoparticles (200 μL, 1 mg mL⁻¹). White circles indicate the distribution difference between the tumor (circle 1), liver (circle 2), and normal tissue (circle 3).

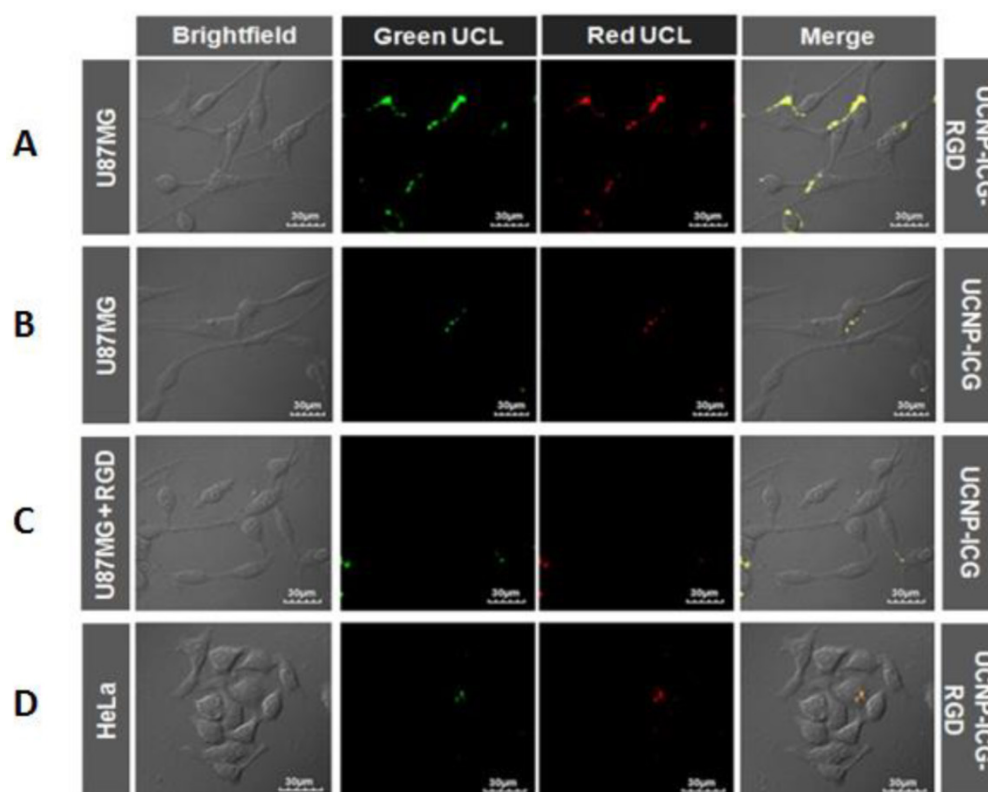


Figure 4. Confocal UCL images of U87MG cells incubated with (A) UCNP-ICG-RGD at 37°C, (B) UCNP-ICG, (C) UCNP-ICG-RGD in the presence of unlabelled RGD. (D) HeLa cells were incubated with UCNP-ICG-RGD (300 µg mL⁻¹). The green and red UCL emission was collected at 530 ± 30 nm and 640 ± 30 nm, respectively.

Targeted UCL imaging

To obtain real-time dynamic imaging information and accurate diagnosis results, a combination of CT and optical imaging modalities is required. Thus, UCL imaging was studied at both the cell and small-animal levels to investigate the optical performance of the UCNP-ICG-RGD.

In vitro: The UCL properties of the CsLu₂F₇-based nanoparticles were compared with those of NaLuF₄-based nanoparticles. The results suggested that the UCL intensity of CsLu₂F₇-based UCNP was slightly weaker than that of NaLuF₄-based nanoparticles. However, the slight difference may not influence the application of UCNP for optical imaging. UCL targeted imaging of UCNP-ICG-RGDs *in vitro* was investigated using a laser scanning upconversion luminescence microscope equipped with CW excitation at 980 nm [47]. As shown in Figure 4A, a strong UCL signal was observed in U87MG cells under CW excitation at 980 nm, whereas HeLa cells showed weak luminescence (Figure 4D). In addition, bright-field images of the cells were obtained. When the UCL and bright field images were merged, UCL was found to originate from the surface of U87MG cells, which was attributed to the highly specific interaction between RGD on the UCNP-ICG-RGDs and integrin $\alpha_v\beta_3$ on U87MG cells.

In contrast, both U87MG cells incubated with UCNP-ICGs without RGD (Figure 4B) and the cells in the competition experiment (Figure 4C) showed weak signals in the UCL images, suggesting non-specific binding of these nanoparticles to the cells. These results demonstrated that UCNP-ICG-RGDs selectively accumulated on the surface of U87MG cells with high integrin $\alpha_v\beta_3$ expression; they can therefore be used as specific agents for targeted imaging of U87MG cells.

In vivo: We next performed *in vivo* imaging using UCNP-ICG-RGDs to specifically target tumors overexpressing integrin $\alpha_v\beta_3$. The same mice used for CT imaging were transferred to the UCL system and imaged using a modified UCL *in vivo* imaging system. Under excitation with a CW 980 nm laser, an intense UCL signal was observed in mice injected with UCNP-ICG-RGDs (Figure 5A). Tissues were dissected from these mice, and a high UCL signal was observed in the liver, spleen, and tumor (Figure 5B). In particular, the region of interest analysis of the UCL signal ($\lambda_{em} = 800 \pm 12$ nm) revealed a high signal-to-noise ratio between the tumor and background. These results suggest that UCL imaging of tumors using UCNP-ICG-RGDs, an efficient label, was successful because of the active targeting ability.

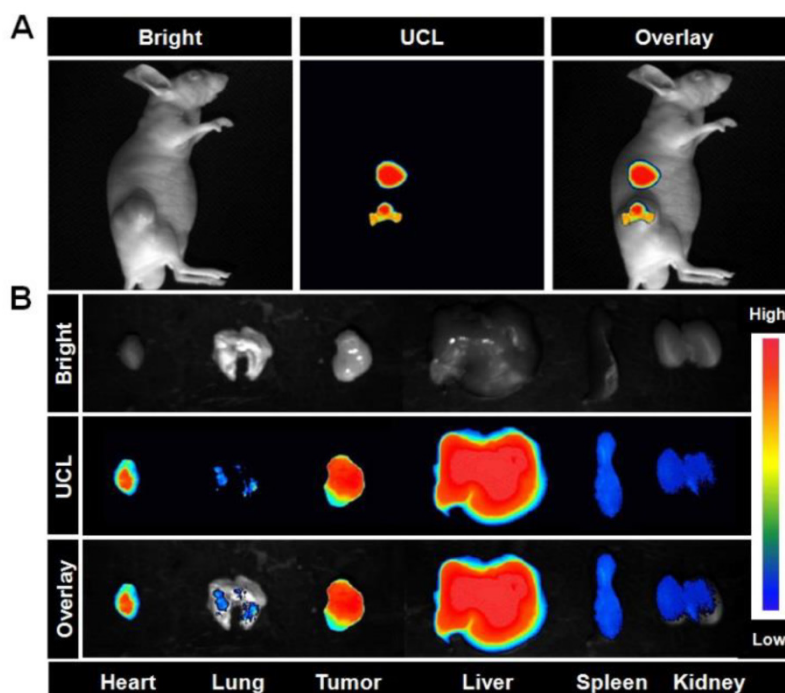


Figure 5. (A) *In vivo* UCL images of the mice bearing U87MG tumors after intravenous injection of UCNP-ICG-RGD (200 μL , 1 mg mL^{-1}). (B) UCL images of tissues (heart, lung, tumor, liver, spleen, and kidney) dissected from the mice. Bright field, UCL, and overlay images were acquired under the same conditions (power $\sim 80 \text{ mW cm}^{-2}$).

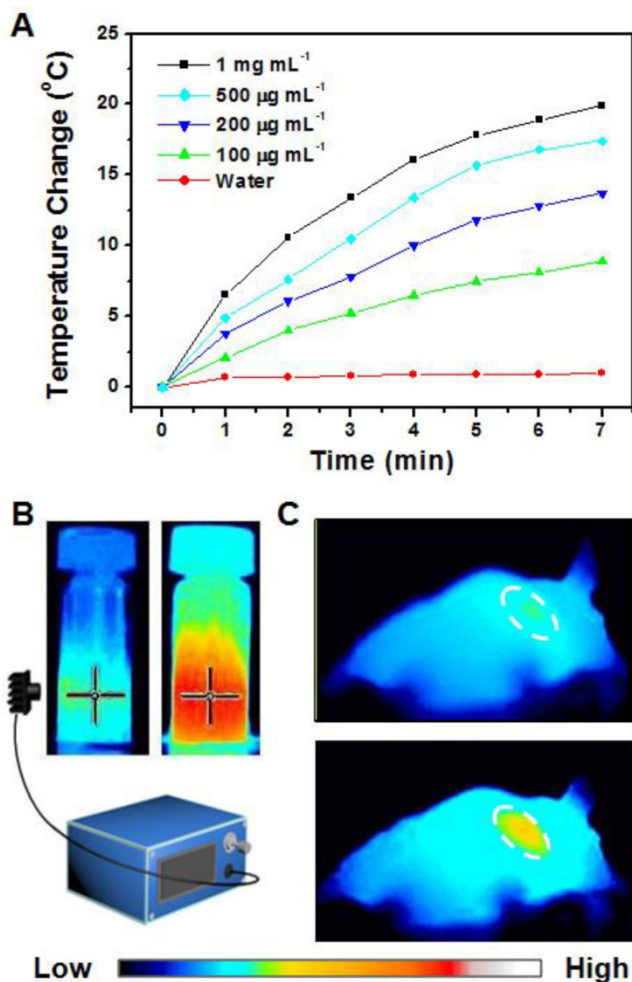


Figure 6. (A) Photothermal imaging was investigated by monitoring UCNP-ICG-RGD solutions (100-1000 $\mu\text{g mL}^{-1}$) at different time intervals irradiated by a NIR laser (808 nm, 0.5 W cm^{-2}). (B) Heating rate of UCNP-ICG-RGD. (C) Photothermal imaging of nude mice injected with UCNP-ICG-RGD solutions irradiated by an 808 nm laser pre- (top) and post- (bottom) injection.

Targeted photothermal imaging

Overheating may damage surrounding tissues, increasing the potential danger of synergistic therapy. Apart from CT and UCL imaging, photothermal imaging can also provide information regarding the progress of therapy, particularly for monitoring temperature. Thus, photothermal imaging was also studied.

In vitro: The UCNP-ICG-RGD solution (100-1000 $\mu\text{g mL}^{-1}$) was exposed to an NIR laser (808 nm, 0.5 W cm^{-2}). The color of the photothermal images changed upon NIR irradiation (Figure 6B). The temperature of the solution increased with increase in concentration and time (Figure 6A). These results indicate that UCNP-ICG-RGDs can be used as a photothermal agent for further bioapplication.

In vivo: Based on the determination of the tumor location in mice, the tumor photohyperthermic effect of the ICG-containing PTT coupling agent was further evaluated. The UCNP-ICG-RGD-induced photothermal cancer therapy *in vivo* was studied using U87MG tumor-bearing mice. Photothermal imaging was used to record the temperature change

in the tumor. Nude mice ($n = 5$) were intravenously injected with the phosphate-buffered saline solution containing UCNP-ICG-RGDs ($200 \mu\text{L}$, 1 mg mL^{-1}) and exposed to an 808 nm laser (0.5 W cm^{-2}). As shown in Figure 6C, the surface temperature of the tumor showed a rapid increase from 31.2°C to 48.8°C with no obvious temperature change in the surrounding tissues. This result indicates that UCNP-ICG-RGD can be applied to monitor the temperature change of the tumor region without damaging the surrounding tissues.

Targeted therapeutic efficacy

Following multifunctional imaging, the tumor location can be determined. To demonstrate that UCNP-ICG-TOS-RGD is a novel nanoplatform that can be used for integration of cancer diagnosis and

synergistic treatment, the therapeutic effect should also be determined.

Chemotherapy efficacy *in vitro*: Based on the conjugation of amino groups on PEG and carboxyl groups on α -TOS, the chemotherapy drug (α -TOS) was conjugated to the nanoparticles to yield α -TOS-conjugated UCNP (UCNP-ICG-TOS-RGD) for chemotherapy (Scheme 1). The UV-vis-NIR spectrum was used to ensure that $\sim 2.02 \times 10^{-5} \text{ mol } \alpha\text{-TOS}$ was covalently attached to per gram nanoparticle, because the apparent absorption peaks at 260 nm were associated with the absorption of free α -TOS (Figure S17). Moreover, the absence of supernatant absorption indicated that no leaching of ICG and α -TOS occurred from the UCNP-ICG-TOS-RGD (Figure S18 and S19). For chemotherapy applications, it is essential to confirm that α -TOS attached to the UCNPs is

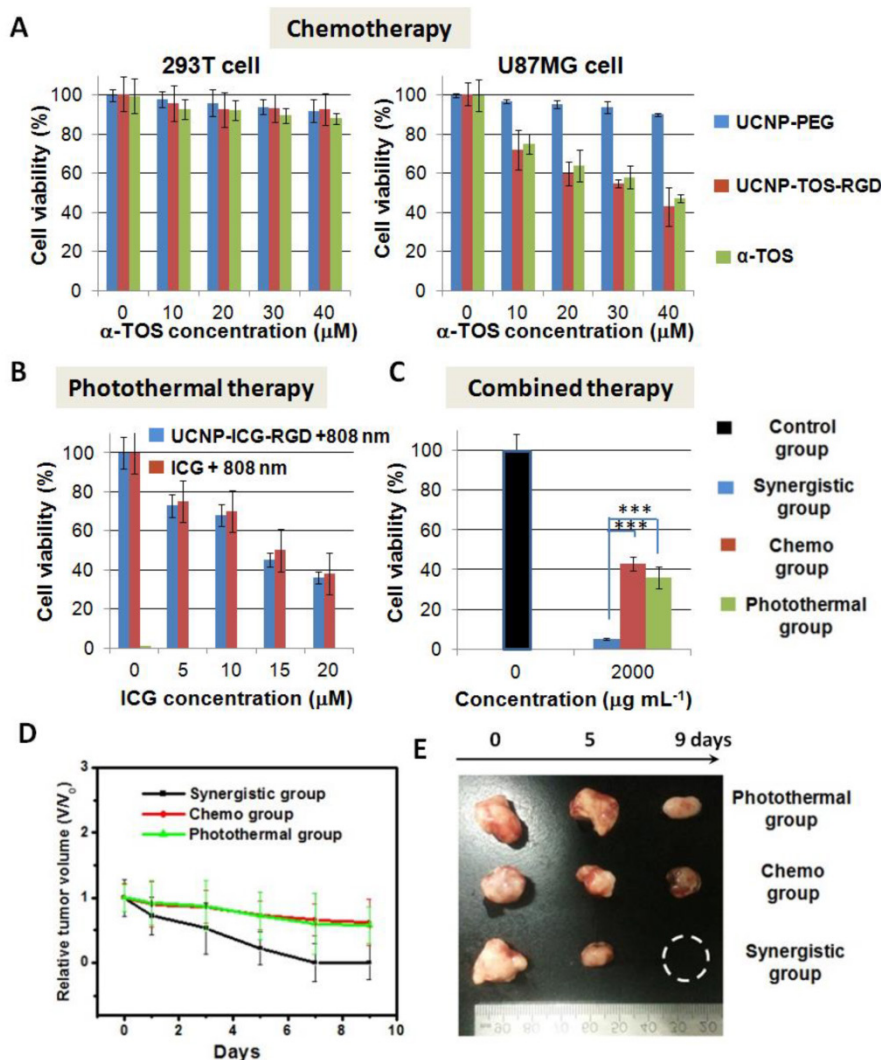


Figure 7. (A) Viability of 293T cells and U87MG cells cultured with medium containing UCNP-PEG, UCNP-TOS-RGD, and free α -TOS at different α -TOS concentrations (0–40 μM). (B) Viability of U87MG cells cultured with medium containing UCNP-ICG-RGD and free ICG at different ICG concentrations (0–20 μM) upon irradiation at 808 nm laser. (C) Viability of U87MG cells with medium containing UCNP-ICG-TOS-RGD upon irradiation at 808 nm laser (Synergistic group), UCNP-TOS-RGD only (Chemo group), and UCNP-ICG-RGD upon irradiation at 808 nm laser (Photothermal group). Cells without treatment were used as a control group. Note. $***p < .001$. (D) Growth rates and (E) photographs of mice in Synergistic group, Chemo group, and Photothermal group.

therapeutically active and has a targeted therapy effect. The therapeutic activity of the developed UCNP-TOS-RGD was evaluated using the MTT assay in U87MG (cancer) and 293T (normal) cells. For comparison, UCNP-PEG and free α -TOS were also tested. As shown in Figure 7A, the inhibitory effect of UCNP-TOS-RGD on U87MG cells was significantly higher than that of UCNP-PEG and was slightly lower than that of free α -TOS at the concentration of 10–40 mM. In contrast to U87MG cells, 293T cells showed significantly higher viability (>90%) under the same treatments (Figure 7A). These results indicated that UCNP-TOS-RGD selectively inhibits cancer cell growth, but has no significant influence on normal cells.

PTT efficacy *in vitro*: To assess PTT, the medium containing UCNP-ICG-RGD was used to incubate U87MG cells irradiated with an 808 nm laser (0.5 W cm^{-2}). As shown in Figure 7B, the viability of U87MG cells, cultured with UCNP-ICG-RGDs and subjected to irradiation, was slightly lower than that of cells cultured with ICG under the same conditions. These data indicate that UCNP-ICG-RGDs have excellent targeted properties and photothermal therapeutic efficacy in cancer cells and should therefore be further analyzed.

Synergetic therapy efficacy *in vitro*: To evaluate the synergetic anticancer effect, U87MG cells cultured with UCNP-ICG-TOS-RGDs and exposed to an 808 nm laser were studied as the experimental group (Synergetic group: UCNP-ICG-TOS-RGD + 808 nm). Control groups were also evaluated (Chemo group: UCNP-TOS-RGD; Photothermal group: UCNP-ICG-RGD + 808 nm). Cell viability without treatment was used as the control (Figure 7C). Compared with chemotherapy only and PTT only, synergetic therapy showed a substantial advantage for eliminating cancer cells ($p < 0.05$). These results indicate that the UCNP-ICG-TOS-RGD combined with NIR laser irradiation is a useful synergetic chemo-photothermal therapy agent for the anticancer biological application.

Synergetic therapy efficacy *in vivo*: The *in vivo* therapeutic efficacy of UCNP-ICG-TOS-RGD-induced synergetic chemo-photothermal treatment was determined in a small-animal model. Four groups consisting of five tumor-bearing mice each were used in our experiment. The synergetic therapy group consisted of mice bearing the U87MG tumor injected with UCNP-ICG-TOS-RGD and exposed to an 808 nm laser (UCNP-ICG-TOS-RGD + 808 nm). Furthermore, two control groups and a blank group were designed: Chemo group (UCNP-TOS-RGD), Photothermal group (UCNP-ICG-RGD + 808 nm), and blank group (fresh medium). The blank group had a higher tumor

growth rate than that of the Synergetic group and two control groups (Figure S20). As shown in Figure 7D, the tumors in the Synergetic group shrank dramatically, whereas tumors in the other two control groups were partially reduced in size. The relative tumor volume (V/V_0) was reduced to zero for the Synergetic group within 9 days of treatment. In contrast, tumors in the control groups shrank slowly, with the V/V_0 reaching as high as 0.6 (Figure 7E). The synergistic effect may contribute to the PTT-induced enhanced permeability of anticancer drugs, by changing the microenvironment of the tumor region and increasing the concentration of anticancer drugs [48–49]. These results indicate that UCNP-ICG-TOS-RGD is a powerful synergetic chemo-photothermal therapy agent for the *in vivo* treatment of cancer.

Conclusion

Previous reports have described upconversion of nanoparticles composed of common alkali metals (Li, Na, or K). In this study, we used cesium (Cs), which has a higher X-ray absorption coefficient than other common alkali metals, to synthesize Cs-based UCNPs using a typical solvothermal method. This multifunctional imaging-therapeutic nanoplatform was then modified with a targeting moiety and therapeutic agents for potential clinical applications. The reported nanoplatform entailed the functions of UCL and CT diagnosis as well as synergetic chemo-photothermal therapy. More importantly, the nanoplatform displayed low *in vivo* toxicity. Our results demonstrated that Cs-based UCNPs exhibited excellent CT performance, which was superior to that of other alkali metals-based UCNPs. Furthermore, UCNP-ICG-TOS-RGDs afforded specific targeted therapy of cancer cells but not normal cells because of α -TOS, a non-common chemotherapeutic drug, and the targeting moiety, RGD. The encouraging results observed in the small animal model warrant further investigations using this multifunctional nanoplatform for its potential use in cancer theranostics.

Supplementary Material

Supplementary tables and figures.

<http://www.thno.org/v06p1491s1.pdf>

Abbreviations

UCL: upconversion luminescence; CT: computed tomography; UCNP: upconversion nanoparticles; PTT: photothermal therapy; NIR: near infrared; RDG: c(RGDFK); OA: oleic acid; ODE: 1-octadecene; ICG: indocyanine green; α -TOS: alpha-tocopheryl succinate; sulfo-NHS: N-hydroxysuccinimide sodium

salt; EDC: 1-ethyl-3-(3-dimethylaminopropyl) carbodiimide hydrochloride; HeLa: human cervical carcinoma; U87MG: human glioblastoma; HEK 293T: human embryonic kidney epithelial cell line.

Acknowledgements

The authors thank Fuyou Li and Xingjun Zhu from Fudan University for the UCL imaging *in vitro* and *in vivo*. The authors thank the funding of National Natural Science Foundation of China (21301121), Scientific Research Base Development Program of the Beijing Municipal Commission of Education (KM201410028008), Beijing Municipal Science & Technology Commission (Z131103002813097), and the Project of Construction of Innovative Teams and Teacher Career Development for Universities and Colleges under Beijing Municipality (IDHT20140512).

Competing Interests

The authors have declared that no competing interest exists.

References

- [1] Liu YL, Ai KL, Lu LH. Nanoparticulate X-ray computed tomography contrast agents: From design validation to *in vivo* applications. *Acc. Chem. Res.* 2012;45(10):1817-27.
- [2] Zhou J, Liu Z, Li FY. Upconversion nanophosphors for small-animal imaging. *Chem. Soc. Rev.* 2012;41(3):1323-49.
- [3] Zhou J, Liu Q, Feng W, Sun Y, Li FY. Upconversion luminescent materials: Advances and applications. *Chem. Rev.* 2015;115(1):395-465.
- [4] Liu XW, Deng RR, Zhang YH, Wang Y, Chang HJ, Huang L, et al. Probing the nature of upconversion nanocrystals: Instrumentation matters. *Chem. Soc. Rev.* 2015;44(6):1479-508.
- [5] Li XM, Zhang F, Zhao DY. Lab on upconversion nanoparticles: Optical properties and applications engineering *via* designed nanostructure. *Chem. Soc. Rev.* 2015;44(6):1346-78.
- [6] Chen GY, Qiu HL, Prasad PN, Chen XY. Upconversion nanoparticles: Design, nanotechnology, and applications in theranostics. *Chem. Rev.* 2014;114(10):5156-214.
- [7] Liu YS, Tu DT, Zhu HM, Li RF, Luo WQ, Chen XY. A strategy to achieve efficient dual-mode luminescence of Eu³⁺ in lanthanides doped multifunctional NaGdF₄ nanocrystals. *Adv. Mater.* 2010;22(30):3266-71.
- [8] Gai SL, Li CX, Yang PP, Lin J. Recent progress in rare earth micro/nanocrystals: Soft chemical synthesis, luminescent properties, and biomedical applications. *Chem. Rev.* 2014;114(4):2343-89.
- [9] Xiao Y, Hong H, Matson VZ, Javadi A, Xu W, Yang Y, et al. Gold Nanorods Conjugated with Doxorubicin and cRGD for Combined Anticancer Drug Delivery and PET Imaging. *Theranostics* 2012;2(8):757-68.
- [10] Huang XQ, Tang SH, Mu XL, Dai Y, Chen GX, Zhou ZY, et al. Freestanding palladium nanosheets with plasmonic and catalytic properties. *Nat. Nanotechnol.* 2011;6(1):28-32.
- [11] Tian QW, Jiang FR, Zou RJ, Liu Q, Chen ZG, Zhu MF, et al. Hydrophilic Cu₉S₅ nanocrystals: A photothermal agent with a 25.7% heat conversion efficiency for photothermal ablation of cancer cells *in vivo*. *ACS Nano* 2011;5(12):9761-71.
- [12] Xiao QF, Zheng XP, Bu WB, Ge WQ, Zhang SJ, Chen F, et al. A core/satellite multifunctional nanotheranostic for *in vivo* imaging and tumor eradication by radiation/photothermal synergistic therapy. *J. Am. Chem. Soc.* 2013;135(35):13041-8.
- [13] Gu ZJ, Yong Y, Zhou LJ, Yan L, Tian G, Zheng XP, et al. WS₂ nanosheet as a new photosensitizer carrier for combined photodynamic and photothermal therapy of cancer cells. *Nanoscale* 2014;6(17):10394-403.
- [14] Zhou ZG, Kong B, Yu C, Shi XY, Wang MW, Liu W, et al. Tungsten oxide nanorods: An efficient nanoplatfor for tumor CT imaging and photothermal therapy. *Sci. Rep.* 2014;4:3653.
- [15] Wang X, Wang C, Cheng L, Lee ST, Liu Z. Noble metal coated single-walled carbon nanotubes for applications in surface enhanced raman scattering imaging and photothermal therapy. *J. Am. Chem. Soc.* 2012;134(17):7414-22.
- [16] Jin YS, Wang JR, Ke HT, Wang SM, Dai ZF. Graphene oxide modified PLA microcapsules containing gold nanoparticles for ultrasonic/CT bimodal imaging guided photothermal tumor therapy. *Biomaterials* 2013;34(20):4794-802.
- [17] Chen M, Fang XL, Tang SH, Zheng NF. Polypyrrole nanoparticles for high-performance *in vivo* near-infrared photothermal cancer therapy. *Chem. Commun.* 2012;48(71):8934-6.
- [18] Zha ZB, Yue XL, Ren QS, Dai ZF. Uniform polypyrrole nanoparticles with high photothermal conversion efficiency for photothermal ablation of cancer cells. *Adv. Mater.* 2012;25(5):777-82.
- [19] Tao Y, Ju EG, Ren JS, Qu XG. Polypyrrole nanoparticles as promising enzyme mimics for sensitive hydrogen peroxide detection. *Chem. Commun.* 2014;50(23):3030-2.
- [20] Zhou J, Lu ZG, Zhu XJ, Wang XJ, Liao Y, Ma ZF, et al. NIR photothermal therapy using polyaniline nanoparticles. *Biomaterials* 2013;34(37):9584-92.
- [21] Liu YL, Ai KL, Liu JH, Deng M, He YY, Lu LH. Dopamine-melanin colloidal nanospheres: An efficient near-infrared photothermal therapeutic agent for *in vivo* cancer therapy. *Adv. Mater.* 2013;25(9):1353-9.
- [22] Li LY, Liu YX, Hao PL, Wang ZG, Fu LM, Ma ZF, et al. PEDOT nanocomposites mediated dual-modal photodynamic and photothermal targeted sterilization in both NIR I and II window. *Biomaterials* 2015;41(0):132-40.
- [23] Guo M, Mao HJ, Li YL, Zhu AJ, He H, Yang H, et al. Dual imaging-guided photothermal/photodynamic therapy using micelles. *Biomaterials* 2014;35(16):4656-66.
- [24] He XY, Bao XY, Cao HQ, Zhang ZW, Yin Q, Gu WW, et al. Tumor-penetrating nanotherapeutics loading a near-infrared probe inhibit growth and metastasis of breast cancer. *Adv. Funct. Mater.* 2015;25(19):2831-9.
- [25] Yue CX, Liu P, Zheng MB, Zhao PF, Wang YQ, Ma YF, et al. Ir-780 dye loaded tumor targeting theranostic nanoparticles for NIR imaging and photothermal therapy. *Biomaterials* 2013;34(28):6853-61.
- [26] Song XJ, Zhang R, Liang C, Chen Q, Gong H, Liu Z. Nano-assemblies of J-aggregates based on a NIR dye as a multifunctional drug carrier for combination cancer therapy. *Biomaterials* 2015;57(0):84-92.
- [27] Cheng L, Wang C, Feng LZ, Yang K, Liu Z. Functional Nanomaterials for Phototherapies of Cancer. *Chem. Rev.* 2014;114(21):10869-939.
- [28] Qiu LP, Chen T, Öcsoy I, Yasun E, Wu CC, Zhu GZ, et al. A cell-targeted, size-photocontrollable, nuclear-uptake nanodrug delivery system for drug-resistant cancer therapy. *Nano Lett.* 2015;15(1):457-63.
- [29] Yang DM, Dai YL, Liu JH, Zhou Y, Chen YY, Li CX, et al. Ultra-small BaGdF₆-based upconversion nanoparticles as drug carriers and multimodal imaging probes. *Biomaterials* 2014;35(6):2011-23.
- [30] Zhu JY, Zheng LF, Wen SH, Tang YQ, Shen MW, Zhang GX, et al. Targeted cancer theranostics using alpha-tocopheryl succinate-conjugated multifunctional dendrimer-entrapped gold nanoparticles. *Biomaterials* 2014;35(26):7635-46.
- [31] Jalil RA, Zhang Y. Biocompatibility of silica coated NaYF₄ upconversion fluorescent nanocrystals. *Biomaterials* 2008;29(30):4122-8.
- [32] Liu P, Yue CX, Shi BH, Gao GH, Li MX, Wang B, et al. A dextran based sensitive theranostic nanoparticles for near-infrared imaging and photothermal therapy *in vitro*. *Chem. Commun.* 2013;49:6143-5.
- [33] Xiong LQ, Chen ZG, Tian QW, Cao TY, Xu CJ, Li FY. High contrast upconversion luminescence targeted imaging *in vivo* using peptide-labeled nanophosphors. *Anal. Chem.* 2009;81(21):8687-94.
- [34] Jin E, Lu ZR. Biodegradable iodinated polydisulfides as contrast agents for CT angiography. *Biomaterials* 2014;35(22):5822-9.
- [35] Liu H, Wang H, Xu YH, Shen MW, Zhao JL, Zhang GX et al. Synthesis of pegylated low generation dendrimer-entrapped gold nanoparticles for CT imaging applications. *Nanoscale* 2014;6(9):4521-6.
- [36] Zhou J, Lu ZG, Shan GG, Wang SH, Liao Y. Gadolinium complex and phosphorescent probe-modified NaDyF₄ nanorods for T₁- and T₂-weighted MRI/CT/phosphorescence multimodality imaging. *Biomaterials* 2014;35(1):368-77.
- [37] Ma JB, Huang P, He M, Pan LY, Zhou ZJ, Feng LL, et al. Folic acid-conjugated LaF₃:Yb,Tm@SiO₂ nanoprobe for targeting dual-modality imaging of upconversion luminescence and X-ray computed tomography. *J. Phys. Chem. B* 2012;116(48):14062-70.
- [38] Zhang G, Liu YL, Yuan QH, Zong CH, Liu JH, Lu LH. Dual modal *in vivo* imaging using upconversion luminescence and enhanced computed tomography properties. *Nanoscale* 2011;3(10):4365-71.
- [39] Tian G, Zheng XP, Zhang X, Yin WY, Yu J, Wang DL, et al. Tpgs-stabilized NaYbF₄:Er upconversion nanoparticles for dual-modal fluorescent/CT imaging and anticancer drug delivery to overcome multi-drug resistance. *Biomaterials* 2015;40(0):107-16.
- [40] Wang HB, Lu W, Zeng TM, Yi ZG, Rao L, Liu HR, et al. Multi-functional NaErF₄:Yb nanorods: Enhanced red upconversion emission, *in vitro* cell, *in vivo* X-ray, and T₂-weighted magnetic resonance imaging. *Nanoscale* 2014;6(5):2855-60.
- [41] Ni DL, Bu WB, Zhang SJ, Zheng XP, Li M, Xing HY, et al. Single Ho³⁺-doped upconversion nanoparticles for high-performance T₂-weighted brain tumor diagnosis and MR/UCL/CT multimodal imaging. *Adv. Funct. Mater.* 2014;24(42):6613-20.
- [42] Xing HY, Bu WB, Zhang SJ, Zheng XP, Li M, Chen F, et al. Multifunctional nanoprobe for upconversion fluorescence, MR and CT trimodal imaging. *Biomaterials* 2012;33(4):1079-89.
- [43] Zhou J, Zhu XJ, Chen M, Sun Y, Li FY. Water-stable NaLuF₄-based upconversion nanophosphors with long-term validity for multimodal lymphatic imaging. *Biomaterials* 2012;33(26):6201-10.

- [44] He M, Huang P, Zhang CL, Hu HY, Bao CC, Gao G, et al. Dual phase-controlled synthesis of uniform lanthanide-doped NaGdF₄ upconversion nanocrystals *via* an OA/ionic liquid two-phase system for *in vivo* dual-modality imaging. *Adv. Funct. Mater.* 2011;21(23):4470-7.
- [45] Yun S, Peng JJ, Feng W, Li FY. Upconversion nanophosphors NaLuF₄:Yb,Tm for lymphatic imaging *in vivo* by real-time upconversion luminescence imaging under ambient light and high-resolution X-ray CT. *Theranostics* 2013;3(5):346-53.
- [46] Xia A, Chen M, Gao Y, Wu DM, Feng W, Li FY. Gd³⁺ complex-modified NaLuF₄-based upconversion nanophosphors for trimodality imaging of NIR-to-NIR upconversion luminescence, X-ray computed tomography and magnetic resonance. *Biomaterials* 2012;33(21):5394-405.
- [47] Yu MX, Li FY, Chen ZG, Hu H, Zhan C, Yang H, et al. Laser scanning up-conversion luminescence microscopy for imaging cells labeled with rare-earth nanophosphors. *Anal. Chem.* 2009;81(3):930-5.
- [48] Zou LL, Wang H, He B, Zeng LJ, Tan T, Cao HQ, et al. Current Approaches of Photothermal Therapy in Treating Cancer Metastasis with Nanotherapeutics. *Theranostics* 2016; 6(6):762-72.
- [49] Wang TT, Wang DG, Yu HJ, Wang MW, Liu JP, Feng B, et al. Intracellularly Acid-Switchable Multifunctional Micelles for Combinational Photo/Chemotherapy of the Drug-Resistant Tumor. *ACS Nano* 2016;10(3):3496-508.